SCIENCE CHINA
Physics, Mechanics & Astronomy

•Article•

April 2023 Vol. 66 No. 4: 246111
https://doi.org/10.1007/s11433-022-2042-x

A room-temperature magnetic semiconductor from a Co-Fe-Nb-B metallic glass

Yu-Zhang Jiao[1,2], Dmitry V. Louzguine-Luzgin[3,4], Ke-Fu Yao[1], Zheng-Jun Zhang[2], and Na Chen[1,2*]

[1] *Laboratory for Advanced Materials Processing Technology (MOE), State Key Laboratory of New Ceramics and Fine Processing, School of Materials Science and Engineering, Tsinghua University, Beijing 100084, China;*
[2] *Key Laboratory for Advanced Materials (MOE), School of Materials Science and Engineering, Tsinghua University, Beijing 100084, China;*
[3] *Advanced Institute for Materials Research (WPI-AIMR), Tohoku University, Sendai 980-8577, Japan;*
[4] *Mathematics for Advanced Materials-OIL, National Institute of Advanced Industrial Science and Technology (AIST), Sendai 980-8577, Japan*

Received September 5, 2022; accepted November 24, 2022; published online February 10, 2023

Magnetic semiconductors with Curie temperatures higher than room temperature show potential for developing spintronic devices with combined data processing and storage functions for next-generation computing systems. In this study, we present an n-type $Co_{19.8}Fe_{8.6}Nb_{4.3}B_{6.0}O_{61.3}$ magnetic semiconductor with a high Curie temperature of ~559 K. This magnetic semiconductor has a room-temperature resistivity of $\sim 2.10 \times 10^4\ \Omega$ cm and a saturation magnetization of ~76 emu/cm^3. The n-type $Co_{19.8}Fe_{8.6}Nb_{4.3}B_{6.0}O_{61.3}$ magnetic semiconductor was deposited on p-type silicon to form a heterojunction, exhibiting a rectifying characteristic. Our results provide the design principles for discovering high Curie temperature magnetic semiconductors with determined conduction types, which would play an essential role in realizing nonvolatile spin-based transistors that break free from the confines of currently established Si-based information technology.

magnetic semiconductor, ferromagnetic metallic glass, high Curie temperature

PACS number(s): 75.50.Pp, 61.43.Dq, 75.50.Kj

Citation: Y.-Z. Jiao, D. V. Louzguine-Luzgin, K.-F. Yao, Z.-J. Zhang, and N. Chen, A room-temperature magnetic semiconductor from a Co-Fe-Nb-B metallic glass, Sci. China-Phys. Mech. Astron. **66**, 246111 (2023), https://doi.org/10.1007/s11433-022-2042-x

1 Introduction

Magnetic semiconductors (MSs) allow the electrical manipulation of ferromagnetism via spin-charge interaction [1,2]. This phenomenon paves the way for the development of spintronic devices with integrated memory and logic functionalities [3]. To make these revolutionary device concepts a reality, tremendous effort has been put into the development of diluted magnetic semiconductors (DMSs) by introducing magnetic elements into nonmagnetic semiconductors [4-8]. Due to their lower Curie temperatures, few DMS have been reported to display room-temperature electric-field controlled ferromagnetism [9,10].

In contrast to the way for making nonmagnetic semiconductors ferromagnetic, making ferromagnetic metallic glasses (MGs) semiconducting is proven to be effective for creating high Curie temperature MSs [11,12]. Furthermore, voltage control of ferromagnetism was performed in these amorphous MSs (AMSs), further confirming their intrinsically mutual interaction between ferromagnetism and electricity [11]. On the other hand, there exist many MG systems with strong ferromagnetism and Curie temperatures

*Corresponding author (email: chennadm@mail.tsinghua.edu.cn)

much higher than room temperature [13]. As a result, they may serve as precursors for the development of new AMSs mediated by oxygen-induced metal-semiconductor transitions, which could aid in the development of room-temperature MS-based spintronic devices. However, most investigations on this new approach to discovering high Curie temperature MSs have so far concentrated on a single Co-Fe-Ta-B alloy system, although there exist tens of ferromagnetic MG systems [14-26]. Meanwhile, the mechanisms underlying the oxygen induced metal-semiconductor transition and the resultant conduction type remain unknown.

Clearly, determining the parameters that influence the conduction types of these AMSs is imperative for the design and synthesis of new MSs with predicted semiconducting properties. To accomplish this, there is an urgent need to develop more AMSs by appropriately choosing different ferromagnetic MG systems. Similar to the previously reported Co-Fe-Ta-B MG system, a Co-Fe-Nb-B MG system was found to exhibit high thermal stability and a high Curie temperature [27-29]. In order to make a comparison with the existing p-type Co-Fe-Ta-B-O AMS for understanding how oxygen mediates the changes in the conduction mechanism, the Co-Fe-Nb-B MG system was therefore selected as a host to form Co-Fe-Nb-B-O glasses with electrical conduction ranging from metals to insulators. Particularly, a new Co-Fe-Ta-B-O AMS was produced, and its optical, electrical, and magnetic properties were investigated.

2 Experimental

The Co-Fe-Nb-B-O_x (CFNBO$_x$) thin films were fabricated via magnetron sputtering from an alloy target with a nominal composition of $Co_{43}Fe_{20}Nb_6B_{31}$ (at.%) in a pure argon or an argon-oxygen environment. Prior to deposition, the base pressure was of the order of 10^{-5} Pa. The substrate temperature for preparing all the samples is room temperature. The oxygen content of the as-prepared thin films was controlled by adjusting the oxygen partial pressure ratio of the working gas mixture, while the deposition time was controlled at 30 min. We began by conducting systematic experiments to investigate the effects of the oxygen partial pressure ratio and deposition rate on the sample oxygen content. Table 1 contains the detailed experimental parameters, including the oxygen partial pressure ratio and deposition rate. An atomic force microscope (AFM) was used to measure the thickness of the as-prepared thin films. The compositions of the as-deposited thin films, including their oxygen contents, were determined using auger electron spectroscopy. The oxygen content of the sample increases as the oxygen partial pressure ratio and deposition rate increase, as shown in Table 1. Even at zero oxygen partial pressure ratio, the thin film has an oxygen content of ~21.6 at.%, owing mostly to the alloy target sintered with metal powders. Based on these experimental results, we created two additional high-oxygen-content thin films with compositions of $Co_{19.8}Fe_{8.6}Nb_{4.3}B_{6.0}O_{61.3}$ and $Co_{16.0}Fe_{7.4}Nb_{3.8}B_{8.1}O_{64.7}$. Their thickness values are 302.1 ± 2.9 and 315.8 ± 12.8 nm, respectively.

The structures of the thin films were investigated using an X-ray diffractometer (XRD). The optical, electrical, and magnetic properties were measured by using a UV/VIS spectrophotometer (UV-2802PC), a physical property measurement system (PPMS-9T), and a scanning superconducting quantum interference device-vibrating sample magnetometer (SQUID-VSM), respectively.

3 Results and discussion

Figure 1 depicts the XRD patterns of the CFNBO$_x$ samples, documenting their structural evolution with the oxygen content x. The first broad diffraction peaks of all the XRD patterns originate from the substrate SiO_2, as indicated by the red arrows in Figure 1. At oxygen contents less than 36.4 at.%, the CFNBO$_x$ samples exhibit a broad diffraction peak located at 2θ of ~45°, as indicated by black arrows in Figure 1, indicating the formation of a single MG phase. The CFNBO$_x$ samples exhibit a second broad diffraction peak situated at 2θ of ~34° at oxygen contents ranging from 36.4 to 53.8 at.%, as indicated by blue arrows, suggesting the emergence of an extra oxide glass (OG) phase. Namely, dual-phase structures of MG and OG are formed in these CFNBO$_x$ thin films. At oxygen contents above 53.8 at.%, the CFNBO$_x$ samples show only one broad diffraction peak arising from the OG phase. This indicates that the CFNBO$_x$ samples

Table 1 Detailed experimental parameters, thicknesses, and compositions of the as-prepared thin films

Oxygen partial pressure ratio	Deposition rate (nm/min)	Thickness (nm)	Element contents (at.%)
0.00	6.6 ± 0.1	198.1 ± 3.5	$Co_{39.1}Fe_{14.0}Nb_{6.0}B_{19.3}O_{21.6}$
0.10	7.1 ± 0.1	213.6 ± 4.0	$Co_{31.8}Fe_{12.2}Nb_{8.6}B_{21.4}O_{26.0}$
0.17	7.5 ± 0.1	225.0 ± 3.8	$Co_{28.4}Fe_{10.3}Nb_{10.1}B_{14.8}O_{36.4}$
0.23	8.3 ± 0.1	249.0 ± 2.0	$Co_{28.5}Fe_{8.6}Nb_{6.8}B_{9.1}O_{47.0}$
0.24	9.2 ± 0.2	277.2 ± 5.0	$Co_{29.2}Fe_{9.9}Nb_{2.5}B_{4.6}O_{53.8}$
0.25	10.1 ± 0.4	304.5 ± 10.9	$Co_{20.4}Fe_{8.2}Nb_{4.0}B_{8.7}O_{58.7}$

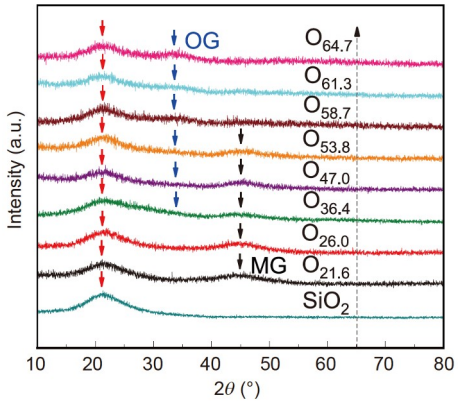

Figure 1 (Color online) XRD patterns of the as-prepared samples showing the structural evolution with the oxygen contents.

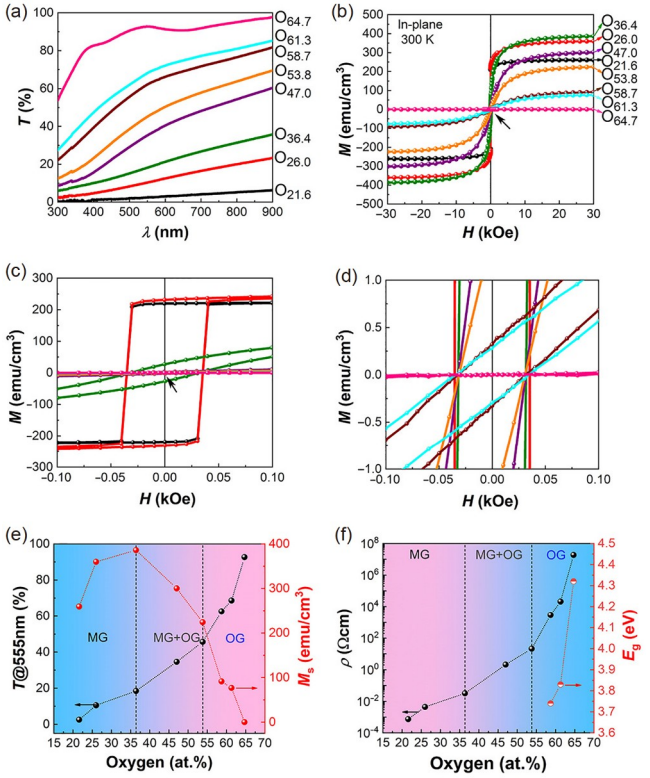

Figure 2 (Color online) (a) Optical transmittance in the visible light range; (b) the magnetization curves; (c) hysteresis loops at low fields as indicated by an arrow in (b); (d) hysteresis loops at low spontaneous magnetization parts as indicated by an arrow in (c); (e) optical transmittance at the wavelength of 555 nm and the saturation magnetization (M_s); (f) room-temperature resistivity and optical bandgaps varying with different oxygen contents in the figure.

eventually transform into single-phase OGs at high oxygen content levels of 58.7-64.7 at.%.

The structural changes with the oxygen contents in the $CFNBO_x$ samples lead to their property changes. Optically, their transmittance in the visible light range increases with increasing oxygen content to 64.7 at.%, as demonstrated in Figure 2(a) and (e). For the transmittance of the as-prepared thin films with different thicknesses, we normalized the data to the transmittance of thin films with a thickness of 100 nm. According to the structural evolution depicted in Figure 1, the optical bandgap gradually opens due to the formation of the OG phase as the oxygen content increases. The volume percentage of this OG phase increases monotonically as the oxygen level increases. Eventually, a single-phase OG is formed when the oxygen content reaches ~58.7 at.%. Hence, the optical transmittance increases monotonically with increasing oxygen content.

The magnetic properties of these $CFNBO_x$ samples are also adjustable with the oxygen contents, in addition to the optical properties. The saturation magnetization (M_s) initially increases with the oxygen content, as seen in Figure 2(b) and (e). When the oxygen content exceeds 36.4 at.%, M_s drops as the oxygen content increases. At the oxygen content of 64.7 at.%, the $CFNBO_{64.7}$ becomes paramagnetic. The magnetization-applied field (M-H) curves of these samples at low field parts, as indicated by black arrows in Figure 2(b) and (c), are shown in Figure 2(c) and (d), respectively. At oxygen contents below 64.7 at.%, the $CFNBO_x$ samples show almost unchanged coercivity values of ~30 Oe (Figure 2(c) and (d)). The reason for the changes in their M_s values with increasing the oxygen content can be understood from two aspects. One is the oxygen addition induced dilution effect, which causes the relative contents of the ferromagnetic metals Co and Fe in the system to decrease. As a result of this dilution effect, the overall ferromagnetism would be reduced. The addition of oxygen, on the other hand, affects local atomic configurations, especially short-range ordering clusters in the system. At low oxygen contents, the added oxygen atoms tend to be attracted by Nb and B due to their higher affinities to oxygen compared with Co and Fe [30]. As a result, the interaction of Nb/B with Co/Fe decreases, enabling more Co-Co, Fe-Fe, and Co-Fe to interact and thereby leading to an increase in their M_s. At an oxygen concentration less than 36.4%, such an increase in M_s prevails over the decrease in M_s due to the dilution effect. As a result, M_s rises to its maximum value, as shown in Figure 2(e). Note that a dual-phase structure starts to emerge in the $CFNBO_{36.4}$ sample, as illustrated in Figure 1. The formation of an OG phase indicates that partial Co and Fe are also starting to oxidize. The contribution from metallic Co and Fe to the ferromagnetism decreases. Hence, the overall ferromagnetism starts to decrease with further increases in the oxygen content.

Increasing the oxygen content increases the room temperature resistivity (ρ) of the $CFNBO_x$ samples from ~7.43×10^{-4} to ~1.88×10^{7} Ω cm (Figure 2(f)), giving a significant resistance differential of 10 orders of magnitude. The optical bandgap (E_g) of the single-phase OGs increases as oxygen content increases (Figure 2(f)). These results in-

dicate that introducing oxygen into the ferromagnetic CFNB MG opens the energy bandgap and enables the formation of various glasses with tunable optical, electrical, and magnetic properties.

When the electrical and magnetic properties of the $CFNBO_x$ samples are combined, it is discovered that the $CFNBO_{58.7}$ and $CFNBO_{61.3}$ OGs are both semiconducting and ferromagnetic. The $CFNBO_{61.3}$ OG is deposited on both p-type Si (P-Si) and n-type Si (N-Si) to form heterojunctions, respectively. The heterojunction of the OG/P-Si is found to show a rectifying feature, confirming its n-type conduction (Figure 3(a)). In comparison, the heterojunction of the OG/N-Si presents a symmetric and slightly nonlinear current-voltage relationship (Figure 3(b)), indicating electrical resistance behavior. Such a nonlinear feature is due to the Schottky barrier formed at the contact between the thin film and the electrode.

Aside from electrical transport properties, the $CFNBO_{61.3}$ OG exhibits negative magnetoresistance (MR) behavior (Figure 3(c)), similar to that seen in a (Ga, Mn)As DMS [31]. The local magnetic moments are gradually aligned by external magnetic fields, which reduces the scattering strength of conduction electrons and therefore decreases the resistance.

The magnetization-temperature relationship determines the Curie temperature of the $CFNBO_{61.3}$ OG to be 559 K. Increasing the temperature over 735 K leads to an increase in the magnetization due to crystallization of the $CFNBO_{61.3}$ OG, comparable to that of the Co-Fe-Ta-B-O MS [11]. Despite having a higher T_c and stronger ferromagnetism, the crystallized Co-Fe-Ta-B-O evolved into a metallic ferromagnet due to a semiconductor-metal transition [16]. This is also quite interesting because such phase transition may enable them to be employed for phase change materials. As a result, it is worth investigating the crystallization behavior of this $CFNBO_{61.3}$ OG as well. As our next step in research, we shall choose such a topic to further our investigation in the future. With its electrical, magnetic, and magnetoelectrical transport properties, the $CFNBO_{61.3}$ OG is confirmed to be an n-type MS with a Curie temperature of ~559 K.

Amorphous metal oxides do have local short-range ordering, despite the lack of long-range order. These non-stoichiometric, short-range ordering clusters exhibit local atomic arrangements over a range of atomic bond lengths and coordination numbers. They could be regarded as a mix of local atomic configurations akin to those of the first-nearest neighboring shells of various metal oxides with the transitional metal cations in various valence states. As a result, the conduction type is controlled primarily by the local atomic structure and valence states of these transition metal cations [32]. In contrast to covalent amorphous semiconductors such as amorphous Si and Ge, the majority of amorphous metal oxides are ionic semiconductors. Their conduction bands, like those of crystalline metal oxides, are primarily dominated by these transition metal orbitals, moving Fermi levels toward the conduction band minima [33]. As a result, the majority of them exhibit n-type conduction, as seen in the $CFNBO_{61.3}$ MS developed in this study. However, replacing Nb with Ta enabled the formation of a p-type $Co_{28.6}Fe_{12.4}Ta_{4.3}B_{8.7}O_{46}$ ($CFTBO_{46}$) MS [11]. Although Nb and Ta have similar atomic radii, they have different outer electronic configurations (Figure 4(a)). It is, therefore, reasonable to believe that Ta and Nb could be the key factors that determine their conduction types.

The primary elements involved in these two systems have different affinities to oxygen due to their various electronic configurations (Figure 4(a)), resulting in different heats of oxide formation, as illustrated in Figure 4(b) [30]. As a result, selective oxidization would occur. The constituents such as the nonmagnetic B, Nb, and Ta in these two systems possess higher heats of oxide formation and prefer to be oxidized first. Normally, the higher heat release results in the formation of more stable oxides. As illustrated in Figure 4(b),

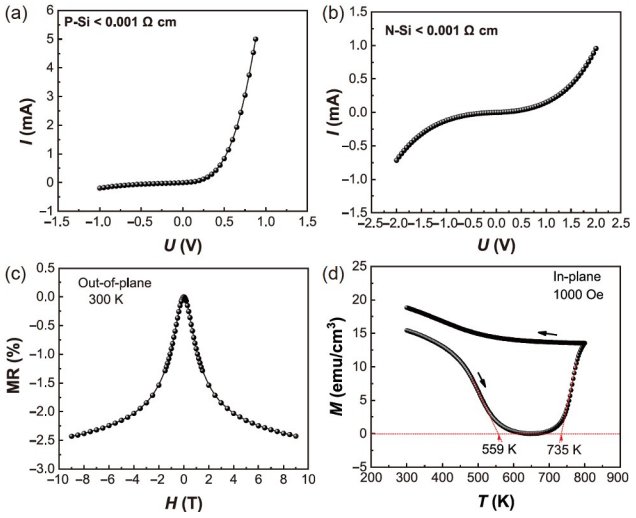

Figure 3 (Color online) (a) The current (I)-voltage (U) curve of the heterojunction based on the $CFNBO_{61.3}$ MS and p-type Si; (b) the current (I)-voltage (U) curve of the heterojunction based on the $CFNBO_{61.3}$ MS and n-type Si; (c) the magnetoresistance (MR) effect of the $CFNBO_{61.3}$ MS; (d) the magnetization-temperature curve of the $CFNBO_{61.3}$ MS, showing the Curie temperature and crystallization temperature.

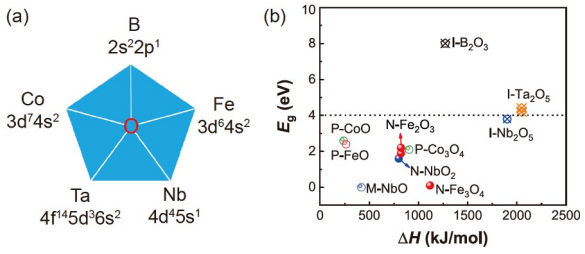

Figure 4 (Color online) (a) Outer electronic configurations of the constituents in the Co-Fe-Ta-B and Co-Fe-Nb-B systems; (b) the heats of different oxide formations and their optical bandgaps.

the most stable oxide states of these three elements have the widest bandgaps, close to or larger than 4 eV. Because of the insulator nature of these B_2O_3, Ta_2O_5, and Nb_2O_5 wide bandgap oxides as denoted by I-B_2O_3, I-Ta_2O_5, and I-Nb_2O_5 [34-36], the conduction types of the Co-Fe-Ta/Nb-B-O systems could be determined primarily by a competition between the local atomic configurations similar to those of p-type Co/Fe oxides and/or n-type Nb oxides [37-39]. As a result, the local atomic structures similar to those of p-type Co oxides (P-CoO/Co_3O_4) and p-type Fe oxides (P-FeO) are supposed to contribute to p-type conduction for the $CFTBO_{46}$ MS, whereas those similar to metallic NbO (M-NbO) and n-type NbO_2 (N-NbO_2) are thought to be the key to switching the p-type $CFTBO_{46}$ MS into the n-type $CFNBO_{61.3}$ MS.

Based on the above discussion, several design principles for producing high Curie temperature MSs with determined conduction types are proposed as follows.

Rule 1 Selecting ferromagnetic MGs with Curie temperatures far above room temperature favors the development of MSs with high Curie temperatures far above room temperature. The intrinsic ferromagnetism, including Curie temperatures and M_s in these MSs, is mediated by charge carriers and is thus dependent on the charge carrier concentration. The addition of oxygen to the ferromagnetic MGs reduces the charge carrier concentration, thereby decreasing the Curie temperature and M_s. As a result, selecting a ferromagnetic MG with a sufficiently high Curie temperature is required for developing an MS with a Curie temperature greater than room temperature. Transition metals such as Co, Fe, and Ni are intrinsically ferromagnetic, based on which ferromagnetic MGs can be formed. Most of them show high Curie temperature values [40-43].

Rule 2 Depending on their valence states, the metal oxides of Co, Fe, and Ni, particularly Fe and Ni, may be either p- or n-type. In order to develop MSs with determined conduction types, the nonferromagnetic metals and metalloids in these ferromagnetic MGs based on Co, Fe, and Ni should be carefully selected. The metal oxides of certain nonferromagnetic metals and metalloids can be classified as insulators, n-type semiconductors, and p-type semiconductors according to their electrical properties, including energy band gaps and electrical resistivity. These elements work in conjunction with the ferromagnetic base metals to affect the conduction types of the amorphous metal oxide semiconductors.

Rule 3 In order to possibly create a p-type MS, it is better to choose nonferromagnetic metals or metalloids, which easily form stable oxide insulators with wide band gaps (see Ta_2O_5 and B_2O_3 in Figure 4(b)). In this situation, the conduction type of the MS would be mainly determined by the ferromagnetic base metals Co, Fe, or Ni. As a result, appropriately altering the atomic ratios of Co, Fe, or Ni could induce p-type conduction in the MS.

Rule 4 To make an n-type MS, it is better to choose nonferromagnetic metals or metalloids, which easily form n-type oxide semiconductors with relatively small band gaps (see NbO and NbO_2 in Figure 4(b)). In this case, it is plausible to presume that the produced MSs could be n-type if the dominating metal valence states of the local atomic configurations are similar to those of the corresponding n-type metal oxides.

Nonferromagnetic semiconductors can be designed using nonferromagnetic MGs in addition to these MSs produced from ferromagnetic MGs. Taking into account the superior mechanical and physical properties of these MGs [44-47], the developed nonferromagnetic semiconductors may possess unique functionalities that can be utilized in electronics as well.

4 Conclusions

In this study, a novel n-type $CoFeNbBO_{61.3}$ MS was developed. This n-type MS exhibited a high Curie temperature of ~559 K, room-temperature resistivity of ~2.10×10^4 Ω cm, and saturation magnetization of ~76 emu/cm^3. In addition, four empirical rules were proposed for designing advanced MSs with known conduction types. Our findings shed light on the conduction mechanisms of these amorphous oxide semiconductors and facilitate the development of room-temperature MS-based spintronic devices.

This work was supported by the National Natural Science Foundation of China (Grant No. 51922053).

1 H. Ohno, Science **281**, 951 (1998).
2 H. Ohno, D. Chiba, F. Matsukura, T. Omiya, E. Abe, T. Dietl, Y. Ohno, and K. Ohtani, Nature **408**, 944 (2000).
3 K. Ando, Science **312**, 1883 (2006).
4 T. Dietl, H. Ohno, F. Matsukura, J. Cibert, and D. Ferrand, Science **287**, 1019 (2000).
5 A. H. MacDonald, P. Schiffer, and N. Samarth, Nat. Mater. **4**, 195 (2005), arXiv: cond-mat/0503185.
6 Y. Matsumoto, M. Murakami, T. Shono, T. Hasegawa, T. Fukumura, M. Kawasaki, P. Ahmet, T. Chikyow, S. Koshihara, and H. Koinuma, Science **291**, 854 (2001).
7 L. Chen, X. Yang, F. Yang, J. Zhao, J. Misuraca, P. Xiong, and S. von Molnár, Nano Lett. **11**, 2584 (2011).
8 H. Wang, S. Sun, J. Lu, J. Xu, X. Lv, Y. Peng, X. Zhang, Y. Wang, and G. Xiang, Adv. Funct. Mater. **30**, 2002513 (2020).
9 Y. Yamada, K. Ueno, T. Fukumura, H. T. Yuan, H. Shimotani, Y. Iwasa, L. Gu, S. Tsukimoto, Y. Ikuhara, and M. Kawasaki, Science **332**, 1065 (2011).
10 F. Xiu, Y. Wang, J. Kim, P. Upadhyaya, Y. Zhou, X. Kou, W. Han, R. K. Kawakami, J. Zou, and K. L. Wang, ACS Nano **4**, 4948 (2010).
11 W. Liu, H. Zhang, J. A. Shi, Z. Wang, C. Song, X. Wang, S. Lu, X. Zhou, L. Gu, D. V. Louzguine-Luzgin, M. Chen, K. Yao, and N. Chen, Nat. Commun. **7**, 13497 (2016).
12 N. Chen, K. Fang, H. Zhang, Y. Zhang, W. Liu, K. Yao, and Z. Zhang, J. Semicond. **40**, 081510 (2019).
13 A. Inoue, and A. Takeuchi, Acta Mater. **59**, 2243 (2011).
14 S. Yin, C. Xiong, C. Chen, and X. Zhang, Phys. Chem. Chem. Phys.

22, 8672 (2020).
15 Y. Zhang, S. Zhao, C. Song, W. Liu, K. Yao, and N. Chen, Mater. Des. **143**, 65 (2018).
16 K. Fang, Y. Zhang, Z. Zhang, and N. Chen, J. Alloys Compd. **797**, 606 (2019).
17 Y. Zhang, L. Zhou, S. Tao, Y. Jiao, J. Li, K. Zheng, Y. Hu, K. Fang, C. Song, X. Zhong, L. Xu, K. F. Yao, Z. Zhang, and N. Chen, Sci. China Mater. **64**, 2305 (2021).
18 X. Wang, X. Li, N. Chen, and T. Zhang, Front. Mater. **9**, 891135 (2022).
19 C. Suryanarayana, and A. Inoue, Int. Mater. Rev. **58**, 131 (2013).
20 K. F. Yao, L. X. Shi, S. Q. Chen, Y. Shao, N. Chen, and J. L. Jia, Acta Phys. Sin. **67**, 016101 (2018).
21 W. Zhang, H. Miao, Y. Li, C. Chang, G. Xie, and X. Jia, J. Alloys Compd. **707**, 57 (2017).
22 Q. Wang, G. Zhang, J. Zhou, C. Yuan, and B. Shen, J. Alloys Compd. **820**, 153105 (2020).
23 F. Fang, C.-P. Zhao, and W. Yang, Sci. China-Phys. Mech. Astron. **54**, 581 (2011).
24 J. Wang, Y. Di, Z. Fang, S. Guan, and T. Zhang, J. Non-Crystalline Solids **454**, 39 (2016).
25 X. Tong, Y. Zhang, Y. Wang, X. Liang, K. Zhang, F. Zhang, Y. Cai, H. Ke, G. Wang, J. Shen, A. Makino, and W. Wang, J. Mater. Sci. Tech. **96**, 233 (2022).
26 Z. Dan, Y. Yamada, and A. Makino, IEEE Trans. Magn. **50**, 2003104 (2014).
27 T. Itoi, and A. Inoue, Mater. Trans. JIM **41**, 1256 (2000).
28 T. Itoi, T. Takamizawa, Y. Kawamura, and A. Inoue, Scripta Mater. **45**, 1131 (2001).
29 T. Gloriant, S. Suriñach, and M. D. Baró, J. Non-Crystalline Solids **333**, 320 (2004).
30 W. F. Gale, and T. C. Totemeier, *Smithells Metals Reference Book* (Elsevier Butterworth-Heinemann, Burlington, 2004).
31 D. V. Baxter, D. Ruzmetov, J. Scherschligt, Y. Sasaki, X. Liu, J. K. Furdyna, and C. H. Mielke, Phys. Rev. B **65**, 212407 (2002), arXiv: cond-mat/0202508.
32 S. Narushima, H. Mizoguchi, K. Shimizu, K. Ueda, H. Ohta, M. Hirano, T. Kamiya, and H. Hosono, Adv. Mater. **15**, 1409 (2003).
33 J. Robertson, J. Non-Crystalline Solids **354**, 2791 (2008).
34 K. A. Stewart, V. Goulouk, D. A. Keszler, and J. F. Wager, Solid-State Electron. **137**, 80 (2017).
35 J. Robertson, J. Vac. Sci. Technol. B **18**, 1785 (2000).
36 T. Onozato, T. Katase, A. Yamamoto, S. Katayama, K. Matsushima, N. Itagaki, H. Yoshida, and H. Ohta, J. Phys.-Condens. Matter **28**, 255001 (2016).
37 H. Lu, Y. M. Zhao, S. E. Saji, X. Yin, A. Wibowo, C. S. Tang, S. Xi, P. Cao, M. Tebyetekerwa, B. Liu, M. Heggen, R. E. Dunin-Borkowski, A. Tricoli, A. T. S. Wee, H. T. Nguyen, Q. B. Yan, and Z. Yin, Appl. Catal. B-Environ. **304**, 121001 (2022).
38 J. M. Xu, and J. P. Cheng, J. Alloys Compd. **686**, 753 (2016).
39 Y. Matsumoto, J. Solid State Chem. **126**, 227 (1996).
40 A. Inoue, A. Makino, and T. Mizushima, J. Magn. Magn. Mater. **215-216**, 246 (2000).
41 R. B. Schwarz, T. D. Shen, U. Harms, and T. Lillo, J. Magn. Magn. Mater. **283**, 223 (2004).
42 Z. Z. Yang, L. Zhu, S. S. Jiang, C. Zhu, Q. H. Xu, Y. Lin, F. G. Chen, and Y. G. Wang, J. Alloys Compd. **904**, 164067 (2022).
43 Z.-B. Jiao, H.-X. Li, Y. Wu, J.-E. Gao, S.-L. Wang, S. Yi, and Z.-P. Lu, Sci. China-Phys. Mech. Astron. **53**, 430 (2010).
44 G. Ding, F. Jiang, X. Song, L. H. Dai, and M.-Q. Jiang, Sci. China-Phys. Mech. Astron. **65**, 264613 (2022).
45 L.-T. Zhang, Y.-J. Duan, D. Crespo, E. Pineda, Y.-J. Wang, J.-M. Pelletier, and J.-C. Qiao, Sci. China-Phys. Mech. Astron. **64**, 296111 (2022).
46 L. Yu, X. Guo, G. Wang, B. Sun, D. Han, C. Chen, J. Ren, and W. Wang, Sci. China-Phys. Mech. Astron. **65**, 264611 (2022).
47 R. Xue, L. Zhao, Y. Cai, J. Yi, J. Cheng, P. Wen, W. Wang, M. Pan, and H. Bai, Sci. China-Phys. Mech. Astron. **65**, 246111 (2022).